Journal of The Electrochemical Society, **159** (9) H752-H757 (2012)
0013-4651/2012/159(9)/H752/6/$28.00 © The Electrochemical Society

Imaging Water-Splitting Electrocatalysts with pH-Sensing Confocal Fluorescence Microscopy

Andrew J. Leenheer and Harry A. Atwater[z]

California Institute of Technology, Thomas J. Watson Laboratories of Applied Physics, Pasadena, California 91125, USA

Hydrogen generation by water electrolysis is promising for energy storage, and imaging the reaction dynamics near a H_2-evolving electrode can provide valuable insights. We utilized laser-scanning confocal fluorescence microscopy to map the product/reactant concentration at a H_2-evolving electrode at micron-scale resolution which identifies areas with fast reaction kinetics. Small concentrations of a pH indicator dye added to the aqueous electrolyte enables ratiometric fluorescence sensing for quantitative pH detection over the range pH 5.3-7.5 and minimally perturbs the local environment. To overcome diffusion limitations, a miniature flow cell was utilized in the microscope to achieve micron-scale resolution in steady state while applying galvanostatic current. We demonstrated the technique using F:SnO_2-coated glass with varied metal catalyst patterns and compositions resulting in clear images of increased pH near areas of high water-reducing activity. Simulations of the pH profiles near the electrolyte-patterned catalyst interface were also performed using the COMSOL finite-element software package to solve the convection/diffusion equations, and the calculation results agreed well with the experimentally-observed fluorescence profiles. Flow cell fluoresecence microscopy shows promise in imaging comparative catalyst activity as well as three-dimensional product/reactant profiles in complex electrode architectures.
 [DOI: 10.1149/2.022209jes]

Manuscript submitted April 23, 2012; revised manuscript received June 19, 2012. Published August 14, 2012.

There is a critical worldwide need for renewable energy sources, but many promising options such as solar or wind energy are intermittent by nature, with limited ability to produce dispatchable power on demand, thus limiting integration of renewables into the power grid. Storing energy in chemical bonds by using renewably-generated electricity to split water could provide a clean and scalable fuel in hydrogen gas or in liquid hydrocarbons after further processing.[1] While current water electrolyzers can provide high efficiencies, they often use expensive catalysts and corrosive electrolytes,[2] motivating research on electrocatalysts that can operate with less overpotential and in neutral aqueous electrolyte. However, traditional catalyst characterization techniques rely on simple current-voltage curves which average the reaction rate over all exposed surface features of the electrode. In contrast, imaging the spatially-resolved reactant or product concentration near the electrode reveals specific areas of high activity and reaction rate resulting from e.g., use of heterogeneous catalysts or high surface area electrode topology. While the evolved gas bubble growth rate can provide a good measure of the local reaction rate,[3] bubbles do not necessarily nucleate near the surface features of interest and can block the flow of reactants. Scanning electrochemical microscopy (SECM) provides submicron resolution and many analytical capabilities, but the presence of the probe significantly perturbs the local environment.[4] Detecting the local pH at a water-splitting cathode indicates the consumed H^+ and evolved OH^- concentrations, indirectly measuring the evolved H_2. pH changes near large platinum electrodes have been quantified by amperometric SECM, identifying both steady-state H_2 evolution as well as transient adsorption and surface oxidation features.[5] By using the potentiometric mode, three-dimensional pH profiles near micron-scale platinum electrodes have also been mapped with SECM with less perturbation[6,7] but require the fabrication of a micron-scale ion selective tip and difficult tip-substrate distance feedback mechanisms.

Changes in pH can be detected not only electrochemically but also through the use of an pH indicator molecule. Conventional colorometric pH indicators can be used[8,9] but require an immobilization strategy if one desires limit the region of analysis to the electrolyte near the active electrode as has been done using thin films and waveguides.[10] Fluorescence-based pH indicators are experimentally more versatile and have been used to spatially image water oxidation[11] and compare electrocatalyst compositions in combinatorial libraries.[12,13] If the indicator dye is present in the bulk electrolyte, dye above area of interest will also be visible resulting in a large background signal, but this contribution can be eliminated with confocal microscopy in the case of a fluorescent indicator.

[z]E-mail: haa@caltech.edu

We utilized a fluorescent pH indicator in an aqueous electrolyte and imaged the pH profile at a hydrogen-evolving electrode using a laser-scanning confocal microscope. Previous studies have developed this technique[14,15] showing three-dimensional diffusion profiles of increased pH in the diffusion layer near cathodic electrodes with resolution on the order of hundreds of microns in quiescent electrochemical cells and provided a semi-quantitative measurement of increased pH based on relative fluorescence intensity. Here we developed a flow cell to reduce the diffusion limitations and reveal three-dimensional product/reactant profiles at micron-scale resolution for varied surface features. The measurement of pH using confocal fluorescence has successfully been applied to refine other electrochemical models such as weak acid transport across a membrane[16] and the actual three-dimensional fluid flow near an impinging microjet.[17] The fluorescent pH indicator molecule is an organic molecule that protonates or deprotonates at a given pK_a value which changes its fluorescence properties. In previous work, fluorescein has commonly been used[14–18] because its absorption and fluorescence emission increases dramatically as pH increases from 4 to 8.[19] However a purely intensity-based measurement is difficult to quantitatively calibrate and is subject to artifacts such as reflective surfaces, dye concentration, laser intensity variations, and shadowing. Therefore in this study we instead used a two-color dye, the fluorescein-derived ratiometric indicator 2′,7′-bis-(2-carboxyethyl)-5-(and-6)-carboxyfluorescein (BCECF) which is often used in biological intracellular pH sensing[20] to enable quantitative pH measurement with few artifacts. The pH profiles are demonstrated on conductive glass patterned with micron-scale metal catalysts, metal catalysts patterned with varied surface area, and a comparison of multiple metals in parallel on one sample that revealed interesting electrochemical activity in conjunction with cyclic voltammetry.

Experimental

Sample fabrication.— Commercial F:SnO_2-coated glass (FTO) was obtained from Pilkington (TEC 15) and polished using Logitech SF-1 colloidal silica on a felt pad to serve as a smooth, transparent, conducting, and non-catalytic substrate cut into pieces about 1-2 cm^2. Electrode patterns were fabricated using standard electron-beam lithography or photolithography techniques followed by metal evaporation and lift-off. For photolithography, a 50-nm anti-reflective polymer layer (Brewer Science WiDe-15B) was spun on the FTO under the photoresist to eliminate back-reflections and overexposure; this layer was removed during the develop in base but remained during the lift-off in acetone. Hence, the bulk of the FTO surface was covered in polymer, with only a small 1-μm region of FTO exposed near the

patterned metal catalyst. After patterning, one corner of the FTO was contacted with a copper wire and silver adhesive paste to complete the working electrode.

Electrochemical cell.— A miniature electrochemical flow cell was made to fit under the microscope objective, and consisted of the planar glass/FTO working electrode, a silicone gasket spacer, and a glass cover slip. The silicone gasket was cut from 0.7-mm thick Press-to-Seal silicone (Grace Biolabs) and provided a watertight seal to the FTO/glass while allowing fast disassembly, cleaning, and reuse of the overall cell. The flow channel was cut from the silicone spacer to about 1-cm long by 1.5-mm wide. Two 1-mm holes were etched in a No. 1.5 cover slip at the flow channel ends, and bent stainless steel tubing was attached using epoxy for fluid input and output ports. The entire top coverslip was epoxied to a copper ring for support, and all epoxy joints were subsequently sealed with RTV-108 silicone. Additionally, a 100 μm-diameter Pt wire was placed between the input and output ports to act as a counter electrode. Galvanostatic current was applied with a Gamry Reference 600 potentiostat in the two-electrode configuration.

Buffered pH calibration solutions over the pH range 4.5-10 consisted of boric acid, citric acid, dipotassium phosphate, sodium sulfate, and sodium hydroxide adjusted to 200 mM total ionic strength in deionized water as well as 20 μM BCECF dye. The electrolyte during analysis consisted of 66 mM sodium sulfate (200 mM ionic strength) and 20 μM BCECF dye in deionized water. The initial bulk pH was adjusted using dilute sulfuric acid or sodium hydroxide. Flow was induced by using a syringe pump to draw electrolyte through the flow cell connected with Tygon or polyethylene tubing and a glass rotameter to measure the flow rate.

Confocal microscope.— A Zeiss LSM710 confocal laser-scanning head was attached to a Zeiss Axio Imager upright microscope equipped with a 20x, 1 NA water-immersion dipping objective lens. This objective provided a maximum field of view of about 500×500 μm. The excitation wavelengths alternated line-by-line between the 458 and 514 nm lines from an argon ion laser adjusted to an intensity that avoided dye saturation or bleaching, though the flow mitigated those effects. The emitted fluorescent light was collected by a photomultiplier tube for wavelengths from 525-720 nm through a confocal pinhole set to 1 Airy unit resulting in a optical slice thickness of about 2.2 micron. Additionally, laser light transmitted through the sample was collected via a transmitted-light photomultiplier tube to show the patterned catalyst location and geometry.

Computer simulation.— Simulations were performed using the convection and diffusion module of COMSOL Multiphysics 4.0 on a personal computer.

Results and Discussion

Ratiometric pH calibration.— The fluorophore BCECF exhibits a pH-sensitive fluorescence excitation spectra and has an isoemissive point at $\lambda = 435$ nm where the fluorescence intensity varies little with pH, whereas the largest change in fluorescence intensity with pH results from excitation at $\lambda = 500$ nm.[20] Thus exciting sequentially with the two different wavelengths and taking the ratio of emitted fluorescence gives a measure of pH which eliminates artifacts resulting from intensity variations present in both signals. The change in fluorescence is due to protonation/deprotonation of the molecule; for BCECF, the exchange is between the tetraanion and pentaanion forms and occurs at $pK_a = 7$. Considering a linear combination of fluorescence of both the tetraanion (basic) and pentaanion (acidic) forms present at a given pH with a first-order dissociation constant for the acid/base equilibria, the pH can be related to the fluorescence emission of two excitation wavelengths $F_{\lambda 1}$ and $F_{\lambda 2}$ as[20]

$$pH = pK_a - \log\left(\frac{R_b - R}{R - R_a} \times \frac{F_{b,\lambda 2}}{F_{a,\lambda 2}}\right) \quad [1]$$

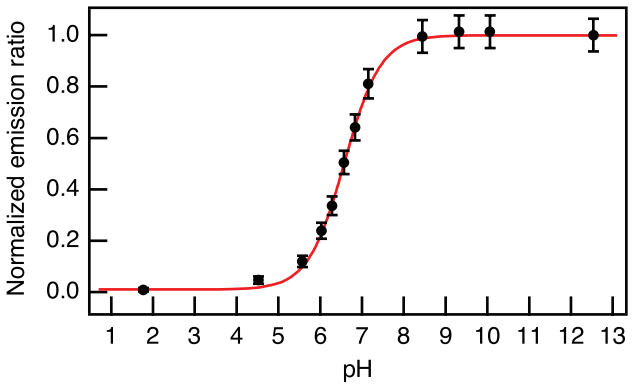

Figure 1. Fluorescence emission ratio 514 nm/408 nm of 20 μM BCECF dye. Circles represent buffered solutions or dilute acid and base endpoints, and solid line shows model using $pK_a = 7.05$ and $F_{b,\lambda 2}/F_{a,\lambda 2} = 2.95$. Error bars indicate standard deviation of ratio largely due to shot noise.

where $R = F_{\lambda 1}/F_{\lambda 2}$ is the measured fluorescence ratio and subscripts a and b indicate values at acidic and basic endpoints, respectively. Only the pK_a of the indicator as well as fluorescence intensities in acid and base are required for calibration of this sigmoidal curve. In the confocal microscope used here, the best available laser excitation wavelengths were at $\lambda_1 = 514$ nm and $\lambda_2 = 458$ nm for the highest signal-to-noise ratio. Fig. 1 shows the relationship between the fluorescence ratio and pH for 20 μM BCECF in calibrated buffer solutions at constant ionic strength as well as endpoints in dilute sulfuric acid and sodium hydroxide. For the model line, the dissociation constant of BCECF was empirically determined to be $pK_a = 7.05$ from the buffered solution at pH 6.5. Clearly, the fluorescence ratio quantitatively determines pH over the range 5.3 to 7.5, but beyond that range the noise and sigmoidal shape allow only upper or lower limits on pH. Other fluorophores with different pK_a values would enable detection over different pH ranges.

Electrochemical cells.— The electrolyte during pH imaging was initially adjusted to pH 5.3 for the most sensitive measure of pH increase during water electrolysis, and 20 μM BCECF dye gave a strong fluorescent signal. Cyclic voltammetry curves (not shown) of this electrolyte showed only peaks related to water, indicating that the BCECF was stable and not prone to strong adsorption over the potential window of water electrolysis.

Initial tests of patterned electrodes in quiescent solution revealed diffusion profiles that approached hundreds of microns within seconds, so we adopted a flow cell geometry to aid convective transport. To test the resolution and demonstrate the technique, a glass/FTO electrode was patterned with a micron-scale cloverleaf of 100-nm thick Au with a 3-nm Cr adhesion layer as shown in Fig. 2a. Encircling each pattern is a small region of exposed FTO, and the rest of the electrode is protected from the electrolyte by WiDe polymer. Fig. 2b shows the pH profile resulting from −4 μA applied to the cloverleaf sample in the flow cell with 0.045 mL/min applied flow while tracking the BCECF fluorescence ratio.

Clear increases in pH are seen near the Au electrocatalyst where hydrogen is being evolved according to the proton reduction reaction

$$H^+ + e^- \rightarrow \frac{1}{2}H_2 \quad [2]$$

or the less facile water reduction reaction

$$H_2O + e^- \rightarrow \frac{1}{2}H_2 + OH^- \quad [3]$$

depending on the local pH and ion concentrations. For near-neutral conditions as used here, the water reduction reaction is dominant. The applied flow is in the laminar flow regime, so products and reactants are swept in the positive x direction as well as diffusing in the y and z directions. In the planar geometry employed here, the pH profile

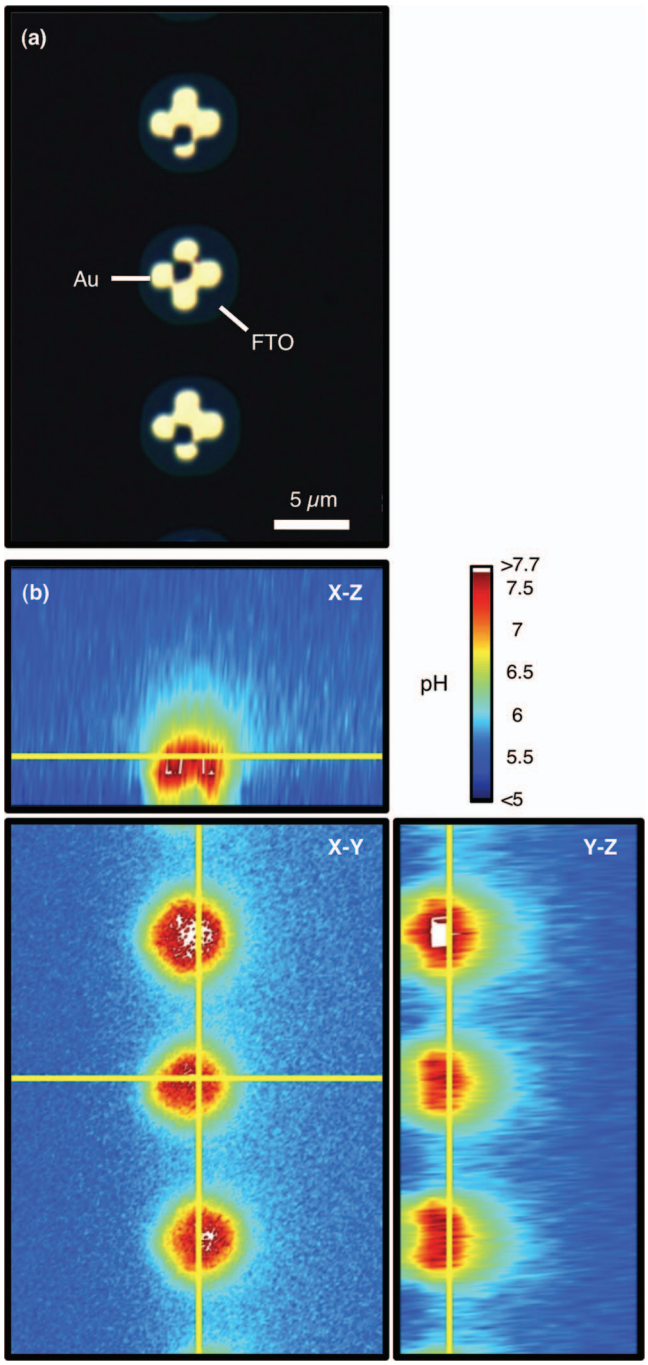

Figure 2. (a) Optical microscope image of patterned Au on FTO and (b) 3D orthonormal projection image of pH with −4 μA applied to sample and fluid flow from left to right. The scale is the same in all images, and the slice locations in the 3D image are shown as yellow lines. pH values above the detection limit are shown as white.

in the z direction is that expected from the diffusion and fluid flow, but the easy three-dimensional imaging capability would be useful for non-planar electrodes or less uniform fluid flows. For this applied current, the flow was sufficient to overcome back-diffusion and reveal the approximate resolution of this technique to be about 5 microns determined from the size of the increased pH features in Fig. 2b. The submicron features in the cloverleaf patterns are not evident primarily due to lateral diffusion. Higher applied current requires a higher flow to maintain resolution. It should be noted that other electrochemical reactions could contribute to the measured pH increase, such as oxygen reduction,

$$\frac{1}{2}O_2 + H_2O + 2e^- \rightarrow 2OH^-, \quad [4]$$

or metal oxide reduction to metal M,

$$M_xO + H_2O + 2e^- \rightarrow xM + 2OH^-. \quad [5]$$

Control experiments showed that de-aerating the electrolyte by purging with Ar gas for 30 minutes showed no effect on the pH profile at a given current, indicating that oxygen reduction was not dominant. Au was chosen as a noble metal catalyst to test this technique because shows little oxidation and little oxide reduction under negative current. Additionally, a control experiment using sodium nitrate supporting electrolyte showed similar pH profiles, so the sulfate ion was unlikely involved in the pH increase.

To demonstrate the sensitivity of this technique to the local current density, a sample was prepared with Au catalyst patterned in 60-μm square patches of hexagonally-packed circles of the same top projected area but varied radius (pitch/radius = 2.4, 62% coverage) by electron-beam lithography with the circle radius varying from 0.2 to 4 μm. The transmitted-light image and pH increase under applied flow and current is shown in Fig. 3 as well as a simulation of the expected pH increase calculated below. Because the indicator dye is most sensitive near its pK_a, it cannot quantitatively measure pH changes above about 1 unit above its pK_a, so any higher values are shown here as white. Since the Au circles were deposited with a finite 50 nm thickness, the sidewall area varied between patches, resulting in area-enhancement factors of at least 1.025, 1.25, 1.063, 1.5, and 1.125 from top to bottom relative to just the top projected area. When negative current was applied to the entire sample, the increased surface areas of the smaller circles is clear in the increased pH profile near those patches. The projected current density effectively increases with local surface area which is clearly seen using this technique. Note that in this case the applied current and flow were chosen to clearly show the differences between the various patches rather than achieve the highest resolution, so the individual circles are not distinct in the pH image.

Fig. 3c shows a simulated three-dimensional finite-element analysis of the pH increase at a water-splitting cathode at the experimental background pH and overall current adjusted to most closely match the experimental image. The actual current density of each patch was then set by the area-enhancement factor. The simulated pH profile shows qualitative agreement with the experimental profiles though with less dependence on circle size. The E-beam lithography and liftoff process likely left rough edges and higher local Au surface area than calculated for the smallest circles. The simulation is useful to compare expected changes in pH with the measured image, and in this case reveals a bigger effect for smaller Au circles than that calculated considering only geometric differences.

The local pH increase can also indicate areas with higher catalytic activity rather than just increased surface area. To demonstrate the dependence on electrocatalyst material, a sample was prepared with islands of different metals patterned by photolithography, and connected electrically in parallel on a FTO substrate. A sample containing 80 nm each of Ag, Pt, Ni, and Au is shown in Fig. 4 as well as the pH increase under current flow before and after an electrochemical cleaning cycle. A video of the pH profile during a cyclic voltammetry cycle is included in the supplemental material link in the online version of this article as Movie S1.[22] First, the FTO shows no activity, confirming its high overpotential for water reduction. Second, the Ag initially shows a very large pH change in Fig. 4b under negative current flow which could be due to reduction of an oxide layer present after the sample fabrication and elevated temperature during photoresist bakes in air. After cycling the sample bias from −1.5 to +1.5 V and back multiple times to clean the surface, Fig. 4c shows no activity from the Ag patch because it has completely oxidized away during the cycle and become insulating. Third, the noble metals Au and Pt show an increase in activity after the cleaning cycles because surface contaminants present from sample fabrication have been oxidized

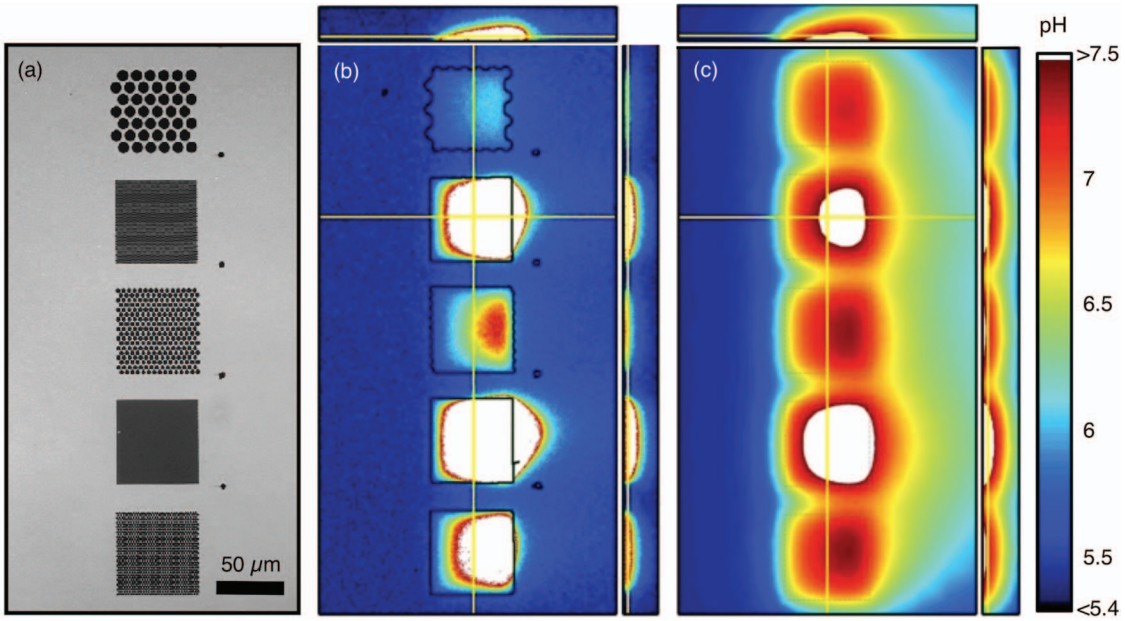

Figure 3. Au circles patterned with varied surface area per patch where the circle radius of each patch from top to bottom is 4, 0.4, 1.6, 0.2, and 0.8 μm. (a) Optical transmission image, (b) 3D orthonormal projection image of pH with −4 μA applied to sample and flow from left to right, and (c) finite element simulation of pH profile.

away, and surface restructuring during the cycles is also a possible reason for the increase.[23] Both before and after the cycling, the Ni patch shows little pH change because its electrochemical activity is less than the other areas during this experiment, so the current tends to flow through the parallel paths that require less overpotential. The present set of metals were chosen based on their different exchange current densities and locations on either side of a 'volcano' plot,[24] and the results seen here more or less agree with the expected trends given the surface conditions and near-neutral pH. Though the precise nature of the surface and quantitative kinetics of the various metals has not been thoroughly characterized here, the relative differences for the water reduction reaction between different materials under the same conditions are clearly seen using this technique.

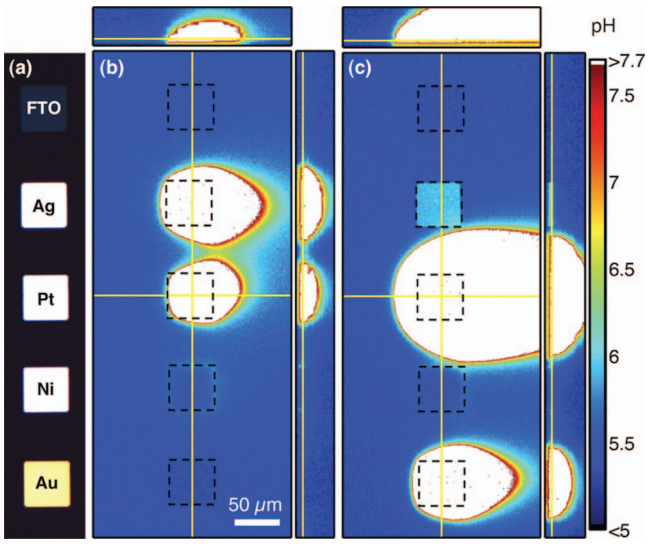

Figure 4. Sample with varied metal electrocatalysts in parallel on FTO with polymer over most of the FTO. (a) Optical brightfield microscope image, showing patches from top to bottom of bare FTO, Ag, Pt, Ni, and Au, (b) 3D orthonormal projection image of pH with −1 μA applied to sample at −1.56 V bias and flow from left to right, and (c) same conditions as in (b) but after cycling sample bias from +1.5 to −1.5 V; here the sample bias was −1.50 V.

The differences in local pH change in Fig. 4 for the different metals of identical geometric area also confirms that the reactions are not mass-transfer limited. The reactant supply and product movement away from each location is the same, yet the various locations display different behavior due to the differences in reaction rates. In this galvanostatic two-electrode experiment, the behavior reveals varied current density of different materials held at the same potential even without a reference electrode. A reference electrode would help determine the working potential but was not included here for a simpler flow cell design in the microscope.

The use of a ratiometric 2-color indicator fluorophore largely eliminates variations due to laser intensity or dye concentration across the image, but care still must be taken near surface features. If the focal plane (confocal slice) is near or below the surface, spectral variations in the surface reflectivity may also change the intensity ratio which was used to calculate the pH. For example, in Fig. 4c the Ag patch has changed to a rough oxide, affecting the intensity ratio and thus indicating a slightly raised pH, but the patch did not show increased pH with increased current, so the lighter color is a slight artifact. For this reason, the x-y data is presented about 2 microns above the sample surface where the confocal slice volume barely includes the surface.

Theory and Calculations

The pH change at an electrode in a cell of arbitrary geometry and with various chemical species can be calculated by finite element techniques to solve the differential equations involved.[14,15,25,26] The governing equation is the Nernst-Planck equation:

$$\frac{\partial c}{\partial t} = \nabla \cdot [D\nabla c - uc + \mu z c \nabla \phi] + R, \qquad [6]$$

where c is the species concentration, t (s) is time, D (m^2/s) is the diffusivity, u (m/s) is the convective flow, μ ($m^2\ V^{-1}\ s^{-1}$) is the electrophoretic mobility, z is the valence, ø (V) is the electric potential, and R (mol $m^{-3}\ s^{-1}$) is a source term accounting for reactions. The expression inside the brackets is the negative concentration flux accounting first for diffusion, second for convection, and third for electromigration. Under the assumptions of steady state conditions, isotropic

diffusivity, high electrolyte conductivity so little potential drop in the electrolyte, and an incompressible fluid, this equation reduces to

$$0 = D\nabla^2 c - u \cdot \nabla c + R \quad [7]$$

which can be readily modeled using finite element simulation.

To model the pH change at a water-splitting cathode near neutral pH, both protons (hydronium ions) and hydroxyl ions must be taken into account as mentioned previously. The applied (negative) current will be distributed between the proton reduction or water reduction reactions depending on the pH, assuming no metal oxide or dissolved oxygen reduction. We further assume that the proton reduction reaction is limited only by the reactant supply at near-neutral pH conditions due to its generally simpler reaction mechanism. For simplicity, the fluorescent pH indicator is assumed to not participate in the electrode reactions or appreciably affect the ion concentrations during the finite element modeling; its effect as a buffer is taken into account after the proton and hydroxyl ion concentrations are calculated. The overall current density is then related to the ion fluxes,

$$\frac{I}{AF} = J_{H^+} - J_{OH^-}, \quad [8]$$

where I is the applied current, A is the electrode area, F is Faraday's constant and the species fluxes J_{H+} and J_{OH-} are in mol m^{-2} s^{-1}. At near-neutral pH, most of the current will be carried by the hydroxyl ion flux and likely reflect the kinetics of the water reduction reaction rather than the proton reduction reaction. The dissociation of water is much faster than diffusion, so local equilibrium will hold for the water dissociation reaction Eq. 3 which has forward and backward rate constants $k_{w,f}$ and $k_{w,b}$ and equilibrium constant $K_W = k_{w,f}/ k_{w,b} = 10^{-14}$ in excess pure water. Correcting for 200 mM ionic strength, $K_W = 10^{-13.73}$. It is easiest to implement this local equilibrium in COMSOL as a reaction for both species with rate

$$R_{H^+} = R_{OH^-} = (k_{wf} - k_{wb}[\mathrm{H}^+][\mathrm{OH}^-]) \quad [9]$$

using $k_{w,f} = 10^{-6.865}$.

The above equations are solved in COMSOL using the Transport of Diluted Species module including convection and diffusion for both protons and hydroxyl ions coupled to the Laminar Flow module to simulate the fluid flow with a no-slip boundary condition along the flow cell walls. The flow cell was modeled in three dimensions over a channel length, width, and height of 1.8, 1.5, and 0.7 mm respectively with the electrocatalyst patches on the bottom of the channel. The ion concentrations in the bulk and on the inlet boundary were set by the initial pH of the electrolyte. At the electrocatalyst patches, the proton concentration was set to 10^{-11} mol/m^{-3} which is approximately zero, representing the facile proton reduction. Based on that boundary condition, the current due to proton reduction at the electrocatalyst patches was subtracted from the applied current, and the remainder of the current was set as an incoming flux of hydroxyl ions. The ionization of water was set as a bulk reaction term for both ions. The diffusivity of protons and hydroxyl ions was set to 9.30×10^{-5} and 4.62×10^{-5} cm^2/s, respectively.[14]

Following the COMSOL simulation, the resulting profiles of proton and hydroxyl ion concentrations were imported in Matlab to calculate the buffering action of the BCECF indicator dye. At each spatial location, we treat the simulated proton concentration as a concentration of strong acid of concentration [A] and the hydroxyl ions as a strong base of concentration [B]. Treating the fluorophore as a weak acid with $pK_F = 7$ and concentration [F], the charge and mass balance result in the equation for $[H^+]$,

$$[\mathrm{A}] + \frac{[\mathrm{F}]K_F}{[\mathrm{H}^+] + K_F} + \frac{K_W}{[\mathrm{H}^+]} = [\mathrm{B}] + [\mathrm{H}^+], \quad [10]$$

which has one positive root used to calculate the solution pH as shown in Fig. 4c, where qualitative agreement is seen with the experimental results. The described approach is very similar to previous calculations of pH involving weak fluorophore buffers,[14,16] with possible slight differences in the treatment of the acid-base equilibria of both water molecules and the fluorophore.

The simulation could be used to calculate the quantitative local current density at a clear surface feature by varying simulated current until the pH profile matches the experiment. The volume and area of an iso-pH surface would make a simple fitness function as long as the fluid flow and fluorophore concentration were carefully controlled in the experiment. However, the patterned catalyst islands of interest must be sufficiently removed from other catalysts so that the diffusion profiles do not overlap in steady state.

Conclusions

We have demonstrated the use of pH-sensing fluorophores to quantitatively image pH gradients resulting from reductive currents in aqueous electrochemical cells. Confocal laser-scanning microscopy was utilized for good signal-to-noise and 3D imaging capabilities. Micron-scale information is possible with the use of a flow cell to overcome diffusion, a resolution which approaches that of scanning probe electrochemical techniques while minimally perturbing the electrochemical conditions. The pH profiles were shown to sensitively respond to variations in both electrocatalyst surface area and inherent catalytic activity. In such an experiment, the area on a substrate with the highest catalytic activity was immediately obvious from the fluorescence profile. This technique could be expanded for use in combinatorial catalyst discovery, where a single substrate was patterned with electrocatalysts with varied composition or growth conditions. In a flow cell, however, the flow should be uniform over the field of view, and pH changes at one spot on the electrode may affect the downstream profiles. Time-resolved images could also provide good resolution without the use of a flow cell. The images presented here were taken in steady state, but the fast laser scanning allows image acquisition in less than a second. Photoelectrodes could be analyzed by switching the illumination sources analogous to a photobleaching experiment, where snapshots of the pH profile are taken after broad illumination of the sample.

The primary limitation of this technique lies in the narrow pH range that is accessible, but other fluorophores could be used with different pK_a values. For example, Oregon Green is another fluorescein derivative with a pK_a of 3-4 where hydrogen-evolution catalysts are typically more active.[27] Alternatively, for the oxygen-evolution reaction, a fluorophore that shows increased fluorescence with decreased pH is quinine,[11,13] or many dyes are quenched in the presence of dissolved oxygen.[28] The added dyes also should interact minimally with the surface to avoid changes in surface chemistry. Due to both diffusion limitations and the diffraction limit of visible light, it is unlikely that the resolution of this technique could be extended below a micron.

Acknowledgments

This material is based upon work performed by the Joint Center for Artificial Photosynthesis, a DOE Energy Innovation Hub, supported through the Office of Science of the U.S. Department of Energy under Award Number DE-SC0004993. We thank V. Ferry and J. McKone for helpful discussions.

References

1. J. Nowotny, C. Sorrell, L. Sheppard, and T. Bak, *Int. J. Hydrogen Energy*, **30**, 521 (2005).
2. S. Grigoriev, V. Porembsky, and V. Fateev, *Int. J. Hydrogen Energy*, **31**, 171 (2006).
3. A. J. Leenheer and H. A. Atwater, *J. Electrochem. Soc.*, **157**, B1290 (2010).
4. A. J. Bard and M. V. Mirkin, editors, *Scanning Electrochemical Microscopy*, Marcel Drekker, Inc., New York, New York (2001).
5. Y.-F. Yang and G. Denuault, *J. Chem. Soc. Faraday T.*, **92**, 3791 (1996).
6. M. Etienne, P. Dierkes, T. Erichsen, W. Schuhmann, and I. Fritsch, *Electroanalysis*, **19**, 318 (2007).
7. B. R. Horrocks, M. V. Mirkin, D. T. Pierce, A. J. Bard, G. Nagy, and K. Toth, *Anal. Chem.*, **65**, 1213 (1993).
8. A. Klimov and G. H. Pollack, *Langmuir*, **23**, 11890 (2007).
9. C. Cabrera, B. Finlayson, and P. Yager, *Anal. Chem.*, **73**, 658 (2001).

10. F. Loete, B. Vuillemin, R. Oltra, D. Chaumont, and E. Bourillot, *Electrochem. Commun.*, **8**, 1016 (2006).
11. J. Vitt and R. Engstrom, *Anal. Chem.*, **69**, 1070 (1997).
12. G. Chen, D. Delafuente, S. Sarangapani, and T. Mallouk, *Catal. Today*, **67**, 341 (2001).
13. E. Reddington, A. Sapienza, B. Gurau, R. Viswanathan, S. Sarangapani, E. Smotkin, and T. Mallouk, *Science*, **280**, 1735 (1998).
14. N. Rudd, S. Cannan, E. Bitziou, L. Ciani, A. Whitworth, and P. Unwin, *Anal. Chem.*, **77**, 6205 (2005).
15. S. Fiedler, R. Hagedorn, T. Schnelle, E. Richter, B. Wagner, and G. Fuhr, *Anal. Chem.*, **67**, 820 (1995).
16. J. Grime, M. A. Edwards, N. C. Rudd, and P. R. Unwin, *Proc. Natl. Acad. Sci.*, **105**, 14277 (2008).
17. E. Bitziou, N. C. Rudd, M. A. Edwards, and P. R. Unwin, *Anal. Chem.*, **78**, 1435 (2006).
18. R. C. Engstrom, S. Ghaffari, and H. Qu, *Anal. Chem.*, **64**, 2525 (1992).
19. R. Sjoback, J. Nygren, and M. Kubista, *Spectrochim. Acta A*, **51**, L7 (1995).
20. N. Boens, W. Qin, N. Basaric, A. Orte, E. M. Talavera, and J. M. Alvarez-Pez, *J. Phys. Chem. A*, **110**, 9334 (2006).
21. G. Grynkiewicz, M. Poenie, and R. Tsien, *J. Biol. Chem.*, **260**, 3440 (1985).
22. See supplementary material at http://dx.doi.org/10.1149/2.022209jes.html.
23. W. Xu, J. S. Kong, Y.-T. E. Yeh, and P. Chen, *Nat. Mater.*, **7**, 992 (2008).
24. J. K. Nørskov, T. Bligaard, A. Logadottir, J. R. Kitchin, J. G. Chen, S. Pandelov, and U. Stimming, *J. Electrochem. Soc.*, **152**, J23 (2005).
25. S. M. Matthews, A. D. Elder, K. Yunus, C. F. Kaminski, C. M. Brennan, and A. C. Fisher, *Anal. Chem.*, **79**, 4101 (2007).
26. S. Cannan, I. Macklam, and P. Unwin, *Electrochem. Commun.*, **4**, 886 (2002).
27. W.-C. Sun, K. R. Gee, D. H. Klaubert, and R. P. Haugland, *J. Org. Chem.*, **62**, 6469 (1997).
28. J. Demas, B. Degraff, and P. Coleman, *Anal. Chem.*, **71**, 793A (1999).